

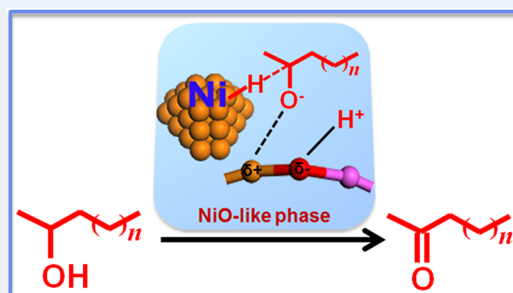
Promoted Synergic Catalysis between Metal Ni and Acid–Base Sites toward Oxidant-Free Dehydrogenation of Alcohols

Hao Chen, Shan He,* Ming Xu, Min Wei,*^{ORCID} David G. Evans, and Xue Duan

State Key Laboratory of Chemical Resource Engineering, Beijing Advanced Innovation Center for Soft Matter Science and Engineering, Beijing University of Chemical Technology, Beijing 100029, P. R. China

Supporting Information

ABSTRACT: In a number of heterogeneous catalysis processes, synergic catalysis of metal and acid–base sites of supports is of vital importance and remains a challenge to obtain largely improved catalytic performance. Herein, an acid–base-promoted Ni nanocatalyst supported on Ni/Al mixed metal oxide (denoted as Ni/NiAl-MMO) was prepared on the basis of the in situ structural topotactic transformation of NiAl-layered double hydroxide (NiAl-LDH) precursor. In situ studies including XRD, Raman, and EXAFS verify that the cubic NiO-like phase (Al³⁺-doped NiO species), with medium-strong acid–base sites (Ni^{δ+}–O^{δ-} pair), are well-distributed in the amorphous Al₂O₃ to form NiAl-MMO support. The concentration of Ni active site and acid–base sites can be simultaneously enhanced by precisely tuning the in situ structural topotactic transformation parameters of LDH precursor as revealed by CO pulse chemisorption, CO₂-TPD, and NH₃-TPD, so as to achieve a promoted synergic catalysis between metal Ni and acid–base sites. The resulting Ni/NiAl-MMO(400) shows largely enhanced catalytic performance (formation rate of 2-octanone: 78.5 mmol g⁻¹ h⁻¹) toward oxidant-free dehydrogenation of 2-octanol to 2-octanone, which is 3.9 times larger than the conventional Ni/Al₂O₃ catalyst (formation rate of 2-octanone: 20.1 mmol g⁻¹ h⁻¹). Studies on the structure–property correlation based on operando time-resolved EXAFS spectra and kinetic isotope effect (KIE) measurements reveal that such an excellent catalytic performance is attributed to the optimized synergic catalysis between Ni⁰ and medium-strong acid–base sites of support, which accelerates the bond cleavage of kinetically key steps: α-C–H and O–H, respectively.



KEYWORDS: layered double hydroxide, synergic catalysis, acid–base sites, dehydrogenation, structure–activity correlation

1. INTRODUCTION

The dehydrogenation of alcohols to carbonyl compounds without an oxidant as hydrogen acceptor is an important and atom-economic synthetic approach for the production of value-added chemicals.^{1–3} Currently, studies on oxidant-free dehydrogenation of alcohols have been focused on the design of supported non-noble metal catalysts with enhanced yields of carbonyl compounds.^{4,5} It has been widely recognized that the acid–base property of the supports normally renders promotion effect on catalytic behavior of immobilized metal catalysts, especially for dehydrogenation reaction.^{6,7} Previous investigations mainly involve changing the type, particle size and shape of metal species as well as the category of acid–base species in supports,^{2,8,9} and the synergic effect between metal sites and acid–base sites may dominate the catalytic performance for alcohols dehydrogenation (e.g., catalytic activity and product selectivity).^{9,10} Recently, Shimizu et al. reported Ni/ θ -Al₂O₃ toward oxidant-free dehydrogenation of alcohols, and they revealed a synergistic catalysis between metal Ni and acid–base sites in this system.¹¹ However, fundamental knowledge on the cooperation of metal sites and acid–base sites as well as their respective contributions to the catalytic behavior is still lacking, and how to achieve promoted synergic catalysis via tuning the microstructure of supported metal catalysts remains

a challenge. Therefore, detailed, systematic research for synergic catalysis between the metal site and acid–base sites of supports based on a catalysis mechanism would be valuable for rational design of new catalysts with largely improved catalytic performance.

Layered double hydroxides (LDHs) are a class of two-dimensional (2D) anion-intercalated materials, which can be generally expressed by the formula [M²⁺_{1-x}M³⁺_x(OH)₂](Aⁿ⁻)_{x/n}·mH₂O. M²⁺ and M³⁺ metal cations are distributed at atomic levels in the hydroxide layers, and Aⁿ⁻ is an anion located in the interlayer region.¹² Recently, LDHs as heterogeneous catalysts or precursors have attracted considerable attention, due to their versatility in chemical composition, structure, and the so-called topotactic transformation property.^{13,14} The most attractive feature of LDHs, as far as catalysis is concerned, is that the LDH precursors containing transition metal cations (e.g., Ni, Co, Fe, and Cu) can be in situ reduced to catalytically active metal nanoparticles anchoring to a mixed metal oxide (MMO) matrix.^{13,14} This preparation strategy for supported metal nanocatalysts not only

Received: December 8, 2016

Revised: February 13, 2017

Published: March 9, 2017

provides a controlled morphology of metal nanoparticles with a high dispersion and stability^{13,14} but also offers a tunable acid–base structure deriving from the MMOs support.^{15,16} This unique property of LDHs materials, therefore, inspires us to explore synergic catalysis between metal and acid–base sites toward oxidant-free dehydrogenation of alcohols.

In this work, an acid–base-promoted Ni nanocatalyst supported on NiAl-mixed metal oxide (denoted as Ni/NiAl-MMO) was successfully prepared on the basis of a precise control over the in situ structural topotactic transformation of NiAl-LDH precursor, which was featured with highly dispersed Ni nanoparticles and medium-strong acid–base sites. A combination study including in situ XRD, in situ Raman, and in situ EXAFS verify that a cubic NiO-like phase (Al³⁺-doped NiO structure) is well-dispersed in amorphous Al₂O₃ matrix, which provides medium-strong acid–base sites (Ni^{δ+}–O^{δ-} pair) confirmed by NH₃-TPD and CO₂-TPD. A promoted synergic catalysis between metal Ni and acid–base sites is achieved via carefully tuning the in situ reduction treatment of NiAl-LDH precursor. A combination study including kinetic isotope effect (KIE) and operando time-resolved EXAFS spectra verifies that the cooperative catalysis of Ni⁰/acid–base sites facilitates the bond cleavage of α -C–H and O–H, accounting for the excellent catalytic performance toward dehydrogenation of 2-octanol. This work demonstrates a successful paradigm for the development of acid–base-site-promoted synergic catalysis between metal and support, based on the unique structural transformation of LDHs precursors.

2. RESULTS AND DISCUSSION

2.1. Structural and Morphological Characterizations.

An acid–base-promoted Ni nanocatalyst supported on Ni/Al mixed metal oxide (denoted as Ni/NiAl-MMO) was prepared on the basis of the in situ structural topotactic transformation of hierarchical NiAl-layered double hydroxide (NiAl-LDH) precursor, similar to a method reported by our group.¹⁷ However, in this work, to achieve a promoted synergic catalysis between metal Ni and acid–base sites of support, a more precise control over the structural topotactic transformation of NiAl-LDH was carried out (e.g., reduction temperature from 400 to 550 °C, heating rate, reducing atmosphere, flow rate and pressure, etc; see [Experimental Section](#)), using an automatic microreactor with an accurate temperature controller. The XRD pattern of hierarchical NiAl-LDH precursor ([Figure 1A](#)) can be indexed to a characteristic feature of layered NiAl-NO₃⁻-LDH phase.¹³ TEM images ([Figure S1a,b](#)) show a solid core and flowerlike LDH shell (~1.5 μ m in height) composed of numerous nanoflakes with a thin thickness (~30 nm). Subsequently, an in situ structural topotactic transformation process was performed over the NiAl-LDH precursor to obtain supported Ni nanoparticles on NiAl-mixed metal oxide (Ni/NiAl-MMO) at 400, 450, 500, and 550 °C, respectively. In situ XRD show that the LDH reflections disappear in these four reduction samples, accompanied by the observation of three weak broad peaks centered at ~37.6°, ~43.7°, and ~63.8° ([Figure 1A](#)) attributed to a cubic NiO-like phase.¹⁸ However, no reflection of Al₂O₃ is observed, indicating an amorphous phase. Moreover, it should be noted that the reflections of cubic NiO-like phase shift slightly to higher 2 θ values compared with the reference sample NiO/Al₂O₃ ([Figure S2A](#)). Correspondingly, the lattice parameter of the NiO-like phase in these four Ni/NiAl-MMO samples (α = 0.4140–0.4155 nm, [Table S1](#)) is significantly smaller than that of the reference sample NiO/

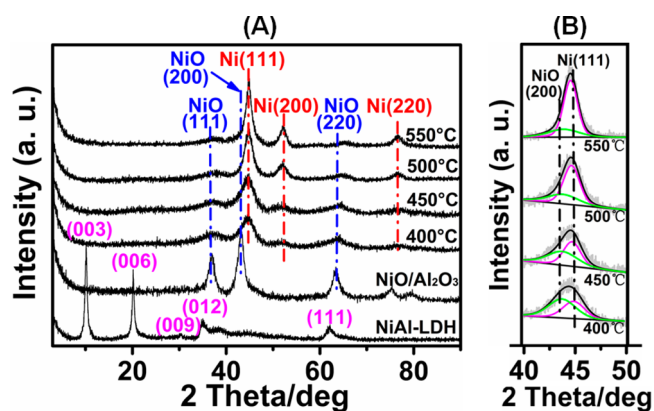


Figure 1. (A) In situ XRD patterns of the NiAl-LDH precursor, NiO/Al₂O₃, and the four reduction samples at 400, 450, 500, and 550 °C, respectively. (B) Enlarged view of in situ XRD patterns within 2 θ 40°–50° selected from A, where each XRD line profile is deconvoluted into two distinct peaks attributed to NiO (200) (green) and Ni (111) (magenta).

Al₂O₃ (α = 0.4172 nm). This is likely because some Ni²⁺ in NiO species are substituted by Al³⁺ with smaller ionic radius (i.e., Al³⁺-doped NiO) and thus result in a lattice shrinking of the NiO-like phase. This would induce a strong interaction between NiO-like phase and Al₂O₃ species¹⁹ and will be further discussed in the following in situ Raman and EXAFS study. In addition, for the four reduction samples, three peaks at 44.8°, 51.9°, and 76.5° assigned to a fcc Ni phase, are also observed. With the increase of reduction temperature from 400 to 550 °C, the peak intensity of metallic Ni enhances gradually while the NiO-like phase shows a reverse tendency; concomitantly, the particle size of metallic Ni calculated by the Scherrer eq ([Table 1](#)) increases from 4.2 to 9.7 nm. This indicates a gradual reduction of NiO-like phase to metallic Ni upon increasing the reduction temperature. As a reference sample, Ni/Al₂O₃ was prepared by immobilizing Ni nanoparticles on amorphous Al₂O₃ support via a traditional deposition method, whose XRD pattern shows a fcc Ni phase with absence of a NiO phase ([Figure S2A](#)).

TEM measurements were performed to investigate the morphology and distribution of Ni species in these four Ni/NiAl-MMO samples ([Figure 2](#)). It is observed that Ni nanoparticles are uniformly dispersed within NiAl-MMO nanoflakes with a high density. Notably, with the reduction temperature rising from 400 to 550 °C, the average size of Ni nanoparticles increases from 3.8 to 8.9 nm, in approximate agreement with the XRD results. In marked contrast, the reference sample Ni/Al₂O₃ is characterized by random packing of Ni nanoparticles with irregular shape and broad particle size distribution (9.3 \pm 2.0 nm, as shown in [Figure S2B](#)). In addition, the Ni/NiAl-MMO(400), Ni/NiAl-MMO(450), Ni/NiAl-MMO(500), Ni/NiAl-MMO(550), and Ni/Al₂O₃ show similar specific surface area (~170 m² g⁻¹) and Ni content (~23.0 wt %) ([Table 1](#)).

To further investigate the sample reducibility and the interaction between NiO-like phase and amorphous Al₂O₃ species, H₂-TPR experiments were performed ([Figure 3A](#)). The TPR profile of NiAl-LDH exhibits two hydrogen consumption peaks: the one at ~270 °C is assigned to the reduction of Ni²⁺ in the lamellar hydroxide structure, and the main peak centered at 500 °C is due to the reduction of highly dispersed NiO-like phase in the strong interaction with

Table 1. Physicochemical Properties of Various Catalysts

sample	BET surface area (m ² g ⁻¹)	Ni species content ^a (wt %)	Ni crystallite size ^b (nm)	mean Ni particle size ^c (nm)	metal Ni dispersion ^e (%)	surface Ni ⁰ concentration ^e (mmol g ⁻¹)	ratio of Ni ⁰ /Ni ²⁺ ^f
Ni/NiAl-MMO(400)	174.7	23.0	4.2	3.8 ± 0.7	25.5	0.450	0.74
Ni/NiAl-MMO(450)	170.1	23.8	5.7	5.3 ± 0.9	18.0	0.402	1.14
Ni/NiAl-MMO(500)	168.4	23.9	7.8	7.5 ± 0.8	12.7	0.378	2.36
Ni/NiAl-MMO(550)	166.1	23.5	9.2	8.9 ± 0.9	10.9	0.360	4.95
Ni/Al ₂ O ₃	170.8	21.8	9.7	9.3 ± 2.0	10.2	0.364	40.7

^aNi species content was determined by inductively coupled plasma–atomic emission spectroscopy (ICP–AES). ^bCrystallite size was determined by XRD with the Scherrer equations. ^cMean Ni particle size was determined by TEM images. ^{d–e}Metal Ni dispersion and surface Ni⁰ concentration were calculated on the basis of the results of CO pulse chemisorption at 200 K (described in Experimental Section). ^fRatio of Ni⁰/Ni²⁺ was calculated on the basis of the results of the linear combination fitting of XANES.

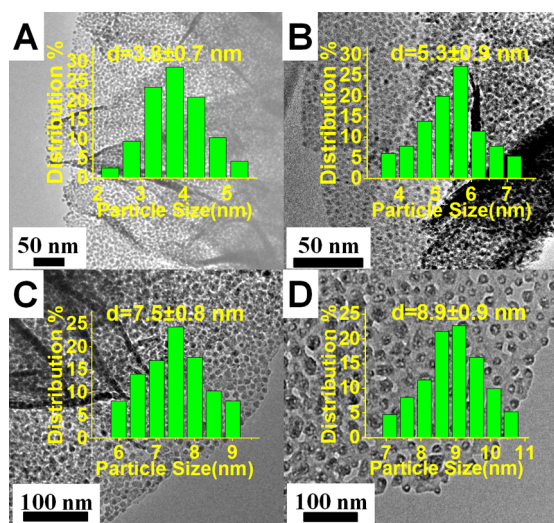


Figure 2. TEM images of (A) Ni/NiAl-MMO(400), (B) Ni/NiAl-MMO(450), (C) Ni/NiAl-MMO(500), and (D) Ni/NiAl-MMO(550). Inset: histogram of size distribution based on more than 500 nanoparticles counted.

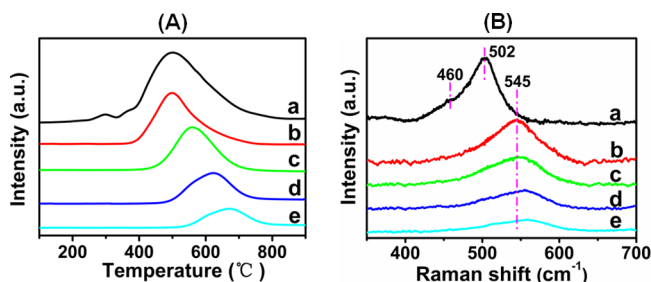


Figure 3. (A) H₂-TPR profiles of (a) NiAl-LDH, (b) Ni/NiAl-MMO(400), (c) Ni/NiAl-MMO(450), (d) Ni/NiAl-MMO(500), (e) Ni/NiAl-MMO(550). (B) Raman spectra of (a) NiO/Al₂O₃, (b) Ni/NiAl-MMO(400), (c) Ni/NiAl-MMO(450), (d) Ni/NiAl-MMO(500), (e) Ni/NiAl-MMO(550).

Al₂O₃.^{20,21} All the four Ni/NiAl-MMO samples show a broad reduction profile: from Ni/NiAl-MMO(400) to Ni/NiAl-MMO(550), the total integrated area of reduction peak (H₂ consumption) decreases gradually. Correspondingly, the percentage of metallic Ni in total Ni species increases from 45% to 82% (Table S2). It is observed that the maximum peaks of TPR profile shift toward higher temperature significantly from Ni/NiAl-MMO(400) to Ni/NiAl-MMO(550), indicating an enhanced interaction between NiO-like phase and Al₂O₃ species, which stabilizes the remaining NiO-like phase. In

contrast, the sample of Ni/Al₂O₃ shows a very low H₂ consumption but a high reduction degree of Ni²⁺ species (96%). Moreover, the surface concentration of Ni⁰ for various samples is determined based on CO pulse chemisorption at 200 K, which decreases from 0.450 to 0.360 mmol g⁻¹ with the reduction temperature rising from 400 to 550 °C (Table 1). This can be attributed to the increased Ni particle size with correspondingly reduced dispersion degree of metal Ni.

In situ Raman measurements were performed to study the chemical environment of surface Ni²⁺ species in these Ni/NiAl-MMO samples (Figure 3B). For the NiO/Al₂O₃ sample, a predominate Raman peak at 502 cm⁻¹ is due to the longitudinal optical (LO) mode of NiO; while its transverse optical (TO) mode at ~460 cm⁻¹ is very weak.^{22,23} In contrast, a single band at ~545 cm⁻¹ is observed for these four Ni/NiAl-MMO samples, which is located between the NiO/Al₂O₃ (502 cm⁻¹) and NiAl₂O₄ (600 cm⁻¹) reported previously.^{24,25} Since the Al₂O₃ phase has no Raman resonance, this peak should be associated with the LO mode of NiO-like phase. This significant shift of LO mode peak toward high frequency relative to NiO/Al₂O₃ is possibly related with the Al³⁺ doping effect (Al³⁺-doped NiO: short-range order structure of Ni_{1-x}Al_xO), and/or the new bond formation (e.g., Ni–O–Al bond), in accordance with the lattice shrinking revealed by XRD. Moreover, the peak intensity of NiO-like phase decreases gradually from Ni/NiAl-MMO(400) to Ni/NiAl-MMO(550), indicating a reduced concentration of surface NiO-like phase. It is thus concluded that NiO-like phase can be described as an intermediate Ni²⁺ species (a solid solution phase) between NiO and NiAl₂O₄, which is highly dispersed in amorphous Al₂O₃ phase with a strong interaction. In contrast, as shown in Figure S3, no Raman resonance is observed in Ni/Al₂O₃ sample, suggesting the absence of surface Ni²⁺ species.

In situ EXAFS spectroscopy was used to reveal the detailed structure of Ni species in various samples. The normalized Ni K-edge XANES spectra for these four samples (Figure 4A), from Ni/NiAl-MMO(400) to Ni/NiAl-MMO(550), show a gradual decrease in the white line intensity compared with NiO reference; however, the edge features for metallic Ni are clearly observed. This indicates the coexistence of metallic Ni and NiO-like phase and a gradual transformation of NiO-like phase to metallic Ni with the increase of reduction temperature. By using a Ni foil (Ni⁰) and a NiO reference (Ni²⁺), the linear combination fitting of XANES was performed to estimate the relative contribution of each Ni state. From Ni/NiAl-MMO(400) to Ni/NiAl-MMO(550), the fitting results indicate that the ratio of Ni⁰/Ni²⁺ increases from 0.74 to 4.95 (Figure 4A and Table 1), which is consistent with the results of H₂-TPR and in situ Raman experiments. In contrast, it is found that

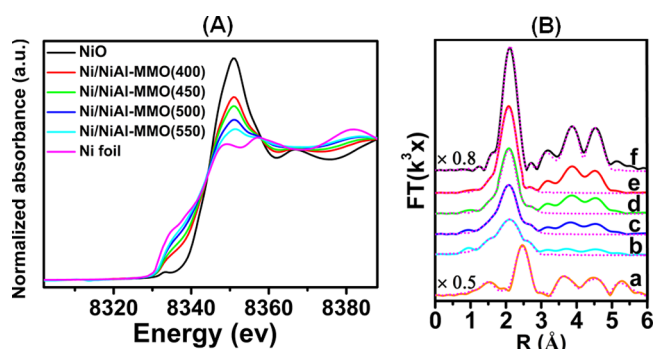


Figure 4. (A) Normalized XANES spectra at Ni K-edge for Ni/NiAl-MMO(400), Ni/NiAl-MMO(450), Ni/NiAl-MMO(500), and Ni/NiAl-MMO(550), respectively. (B) Fourier-transform EXAFS spectra at Ni K-edge for (a) NiO reference, (b) Ni/NiAl-MMO(400), (c) Ni/NiAl-MMO(450), (d) Ni/NiAl-MMO(500), (e) Ni/NiAl-MMO(550), (f) Ni foil (the solid line: experimental data; the dashed line: fitting curve).

metallic Ni is dominant in Ni/Al₂O₃ (97.6% of metallic Ni) by the XANES fitting (Figure S4 and Table 1).

For these four Ni/NiAl-MMO samples, the FT k^3 -weighted EXAFS spectra at the Ni K-edge (the R-space plot) and corresponding curve-fitting results are obtained, and the peaks in the R range of 1–3 Å correspond to the first shell of NiO-like phase, the first shell of metallic Ni and the second shell of NiO-like phase, respectively (Figure 4B). Notably, the R-space plots (Figure 4B) are not phase corrected and thus do not represent the true bond distances. The fitting results including coordination number, bond distance, and Debye–Waller factor are listed in Table S3. It is observed that the first Ni–O shell distance of NiO-like phase (~2.05 Å, Table S3) in Ni/NiAl-MMO samples is smaller than that of NiO reference (2.08 Å) and nanoscaled NiO (2.07 Å) reported in the literature;²⁶ whereas the Debye–Waller factors of both the first Ni–O shell and the second Ni–Ni shell (Ni–O–Ni bond) of NiO-like phase is significantly larger than those of NiO reference (Figure S5 and Table S3) and nanoscaled NiO.²⁶ This can be explained by the Al³⁺ doping and the formation of Ni–O–Al bond: some Al³⁺ substitute for Ni²⁺ in the lattice of NiO to form octahedral Al³⁺, which results in a lattice contraction and a severely distorted octahedral Ni–O environment. Correspondingly, the coordination information about the Ni–Al shell (Ni–O–Al bond) is obtained from the fitting (Table S3). The coordination number of Ni–O shell in NiO-like phase declines from Ni/NiAl-MMO(400) to Ni/NiAl-MMO(550), suggesting a decreased particle size of the NiO-like phase; in contrast, the coordination number of the first Ni–Ni shell in metallic Ni (distance: ~2.48 Å) increases gradually from 4.0 to 9.2, which is attributed to growth of Ni particle size.

2.2. Surface Acid–Base Property of Ni/NiAl-MMO Samples. CO₂ and NH₃-TPD technique have been widely used to probe the surface acid–base properties of solid catalysts,¹¹ which were therefore employed here to correlate the structure and concentration of base/acid site with catalytic performance. For Ni/Al₂O₃ and the four Ni/NiAl-MMO samples, as shown in Figure 5, a broad desorption peak for either CO₂ or NH₃ is observed between 100 and 500 °C. To obtain the distribution of basic/acidic strength and quantitative results, the CO₂-TPD or NH₃-TPD profile is deconvoluted to three peaks according to the desorption temperature, via a Gaussian peak fitting method (Figure 5 and Table 2). The

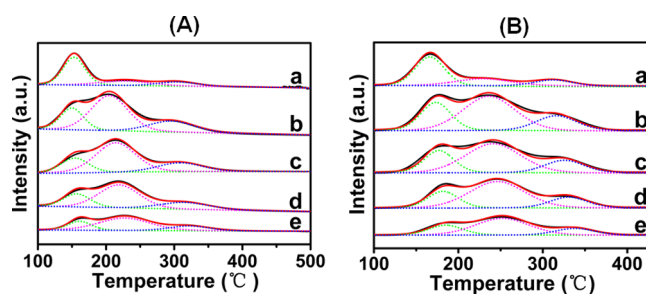


Figure 5. (A) CO₂-TPD profiles, which are deconvoluted into three peaks corresponding to weak base (B_w, green), medium-strong base (B_m, magenta) and strong base (B_s, blue) site. (B) NH₃-TPD profiles, which are deconvoluted into three peaks assigned to weak acid (A_w, green), medium-strong acid (A_m, magenta) and strong acid (A_s, blue) site: (a) Ni/Al₂O₃, (b) Ni/NiAl-MMO(400), (c) Ni/NiAl-MMO(450), (d) Ni/NiAl-MMO(500), and (e) Ni/NiAl-MMO(550).

desorption temperature and area of fitted peak for CO₂-TPD/NH₃-TPD correspond to the strength and quantity of base/acid site, respectively. The deconvoluted CO₂-TPD profiles of all samples display three desorption peaks with maximal temperatures (T_M) in the regions of 140–160 °C, 200–230 °C, 300–340 °C, which are identified as the weak, medium-strong, and strong base site, respectively.^{27,28} In addition, according to previous reports,^{16,28,29} the strong basic site in Ni/NiAl-MMO catalysts is derived from low-coordinated oxygen anion. The NH₃-TPD profiles are deconvoluted to three peaks with T_M in the regions of 160–190 °C, 220–260 °C, 320–360 °C, which are associated with the weak, medium-strong, and strong acid site, respectively.^{6,30} It is observed that desorption peak of the weak base (~155 °C) or weak acid site (~165 °C) for Ni/Al₂O₃ is dominant, with the absence of Ni²⁺ species. In contrast, for Ni/NiAl-MMO samples, both the medium-strong base site and medium-strong acid site are promoted obviously to be predominant in the presence of NiO-like phase. Meanwhile, it should be noted that the concentration of medium-strong base or acid site increases almost linearly with the increment of Ni²⁺ content (Figure S6). This suggests that both the medium-strong base and acid site largely originate from the NiO-like phase. The formation of Ni–O–Al bond (as bridged hetero metal–oxygen bond) causes a lattice shrinking of NiO-like phase and a severely distorted octahedral Ni–O microenvironment, resulting in an increased electron density around O²⁻ (Lewis base site) and correspondingly a decreased electron density at Ni²⁺ (Lewis acid site).^{31,32} Moreover, the coordinatively unsaturated Ni–O structure of NiO-like phase (as shown in EXAFS) facilitate the formation of abundant medium-strong base–acid sites. Overall, from Ni/NiAl-MMO(550) to Ni/NiAl-MMO(400) with enhanced Ni²⁺ content, the total base or acid concentration increases gradually. The results indicate that the NiO-like phase dispersed in amorphous Al₂O₃ intensively affect the basicity and acidity of NiAl-MMO support.

2.3. Catalytic Evaluations toward Oxidant-Free Dehydrogenation of Alcohols and Discussions on Structure–Activity Correlation. To give a deep insight into the synergistic catalysis of metallic Ni and acid–base sites of support, oxidant-free dehydrogenation of 2-octanol was performed as a probe reaction over these Ni/NiAl-MMO samples and Ni/Al₂O₃ at 170 °C (Figure 6 and Table 3). Profiles of 2-octanone yield versus reaction time for various samples are shown in Figure 6A. It can be seen that the Ni/

Table 2. Concentration of Acid and Base Site According to CO₂-TPD and NH₃-TPD Profiles

samples	base sites (mmol g ⁻¹)				acid sites (mmol g ⁻¹)			
	B _{CO₂} ^a	B _W ^b	B _M ^c	B _S ^d	A _{NH₃} ^e	A _W ^f	A _M ^g	A _S ^h
Ni/NiAl-MMO(400)	0.822	0.173	0.481	0.168	0.910	0.215	0.545	0.150
Ni/NiAl-MMO(450)	0.717	0.144	0.437	0.136	0.789	0.175	0.487	0.127
Ni/NiAl-MMO(500)	0.603	0.121	0.369	0.113	0.675	0.151	0.418	0.106
Ni/NiAl-MMO(550)	0.381	0.072	0.244	0.065	0.438	0.097	0.275	0.066
Ni/Al ₂ O ₃	0.370	0.231	0.081	0.058	0.418	0.259	0.101	0.058

^aB_{CO₂} represents the total concentration of base sites, which is calculated on the basis of the results of CO₂-TPD. ^{b-d}B_W, B_M, and B_S are the concentration of weak, medium-strong, and strong base site, respectively, which are calculated on the basis of the results of CO₂-TPD and the deconvoluted TPD profile in the temperature region of 100–500 °C. ^eA_{NH₃} denotes the total concentration of acid sites, which is calculated based on the result of NH₃-TPD. ^{f-h}A_W, A_M, and A_S are the concentration of weak, medium-strong, and strong acid site, respectively, which are calculated on the basis of the results of NH₃-TPD and the deconvoluted TPD profile in the temperature region of 100–500 °C.

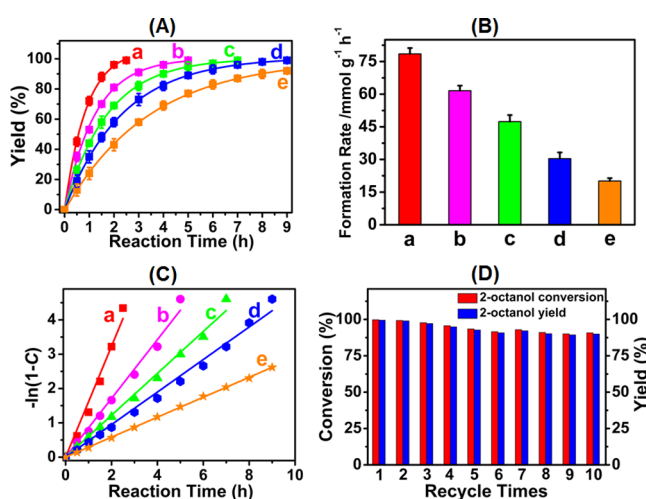


Figure 6. (A) Profiles of 2-octanone yield vs reaction time, (B) the product formation rate at 35% yield of 2-octanone, and (C) first-order kinetic plots for oxidant-free dehydrogenation of 2-octanol: (a) Ni/NiAl-MMO(400), (b) Ni/NiAl-MMO(450), (c) Ni/NiAl-MMO(500), (d) Ni/NiAl-MMO(550), and (e) Ni/Al₂O₃. C represents the conversion of 2-octanol. (D) Catalytic behavior of Ni/NiAl-MMO(400) for oxidant-free dehydrogenation of 2-octanol over 10 consecutive cycles. Reaction conditions: *o*-xylene (6.3 g), 2-octanol (6.3 mmol), *n*-dodecane (3.15 mmol), catalyst (0.05g), 170 °C, 2.5 h, Ar atmosphere.

NiAl-MMO(400) catalyst shows the shortest reaction time (within 2.5 h) to catalyze 100% conversion of 2-octanol to 2-octanone, indicating the highest catalytic activity. The product formation rate at 35% yield of 2-octanone (Figure 6B) obeys the following sequence: Ni/NiAl-MMO(400) (78.5 mmol g⁻¹ h⁻¹) > Ni/NiAl-MMO(450) (61.6 mmol g⁻¹ h⁻¹) > Ni/NiAl-MMO(500) (47.4 mmol g⁻¹ h⁻¹) > Ni/NiAl-MMO(550) (30.4 mmol g⁻¹ h⁻¹) > Ni/Al₂O₃ (20.1 mmol g⁻¹ h⁻¹). A linear relationship is obtained between $-\ln(1 - C)$ and reaction time, indicating the first-order reaction over these four Ni/NiAl-MMO and Ni/Al₂O₃ samples (Figure 6C). The rate constant for Ni/NiAl-MMO samples decreases gradually from 1.62 to 0.47 h⁻¹, much higher than that of Ni/Al₂O₃ (0.29 h⁻¹) (Table 3). The formation rate of 2-octanone for Ni/NiAl-MMO(400) (78.5 mmol g⁻¹ h⁻¹) is 3.9 times larger than that for the conventional Ni/Al₂O₃ catalyst (20.1 mmol g⁻¹ h⁻¹). The catalytic performance of Ni/NiAl-MMO(400) sample is also compared with previously reported catalysts toward oxidant-free dehydrogenation of 2-octanol (Table S4). In addition, oxidant-free dehydrogenation of various alcohols is investigated, and the results are summarized in Table S5. The Ni/NiAl-MMO(400) displays excellent catalytic performance toward the dehydrogenation of other secondary, aromatic, and cycloaliphatic alcohols to the corresponding ketones with high yields. When the Ni/NiAl-MMO(400) catalyst was reused for 10 consecutive cycles, both the conversion and yield decrease by ~10% over 6 consecutive cycles, and then maintain at a stable level, whereas the selectivity of 2-octanone maintains

Table 3. Catalytic Performances of Various Samples for Oxidant-Free Dehydrogenation of 2-Octanol^a

catalysts	surface Ni ⁰ concentration ^b (mmol g ⁻¹)	B _M ^c (mmol g ⁻¹)	A _M ^d (mmol g ⁻¹)	reaction time (h)	yield (%)	first-order rate constants ^e <i>k</i> (h ⁻¹)	formation rate ^f (mmol g ⁻¹ h ⁻¹)	TOF (h ⁻¹) ^g
Ni/NiAl-MMO(400)	0.450	0.481	0.545	2.5	>99	1.62	78.5 ± 2.70	174.4 ± 1.59
Ni/NiAl-MMO(450)	0.402	0.437	0.487	5	>99	0.86	61.6 ± 2.30	153.2 ± 1.33
Ni/NiAl-MMO(500)	0.378	0.369	0.418	7	>99	0.61	47.4 ± 3.00	125.4 ± 3.78
Ni/NiAl-MMO(550)	0.360	0.244	0.275	9	>99	0.47	30.4 ± 2.80	84.4 ± 2.37
Ni/Al ₂ O ₃	0.364	0.081	0.101	9	92	0.29	20.1 ± 1.32	55.2 ± 1.11

^aReaction conditions: *o*-xylene (6.3 g), 2-octanol (6.3 mmol), *n*-dodecane (3.15 mmol), catalyst (0.05 g), 170 °C, 2.5 h, Ar atmosphere. ^bSurface Ni⁰ concentration is calculated on the basis of the results of CO pulse chemisorption at 200 K. ^cB_M denotes the concentration of medium-strong base site. ^dA_M denotes the concentration of medium-strong acid site. ^eFirst-order rate constant (*k*, h⁻¹) is calculated on the basis of the slope of first-order kinetic plots for oxidant-free dehydrogenation of 2-octanol. ^fFormation rate of 2-octanone is calculated on the basis of tangent slope of the yield-reaction time plot at the 35% yield of 2-octanone. ^gTurnover frequency (TOF, h⁻¹) is calculated as formation rate of 2-octanone per surface Ni atoms.

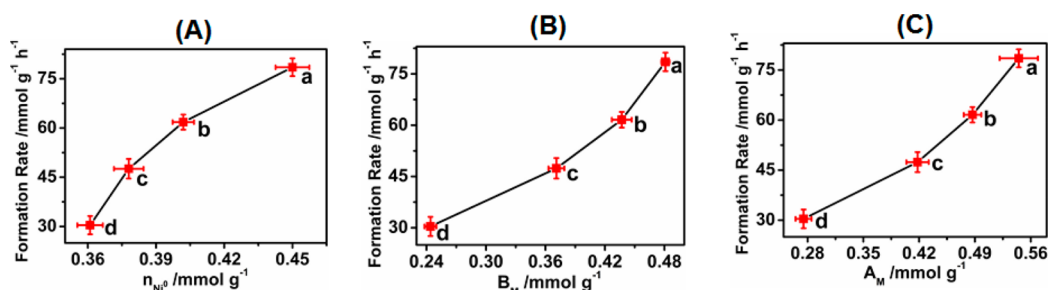


Figure 7. (A) Formation rate of 2-octanone as a function of Ni^0 surface concentration; (B,C) Formation rate of 2-octanone as a function of medium-strong base concentration (B_M) or medium-strong acid concentration (A_M): (a) Ni/NiAl-MMO(400), (b) Ni/NiAl-MMO(450), (c) Ni/NiAl-MMO(500), and (d) Ni/NiAl-MMO(550).

above 99% within 10 cycles (Figure 6D). This could be attributed to a small growth of Ni particles during the first few consecutive cycles, and the XRD pattern and TEM images of the used catalyst after 10 cycles are shown in Figure S7.

To establish a structure–activity correlation for these Ni/NiAl-MMO catalysts, the turnover frequency (TOF) value was measured at the 2-octanone yield of 35% (Table 3). In previous studies, the surface metal site was proposed to be the primary active species in the alcohol dehydrogenation reaction, whereas the acid–base sites of the supports played a promotional role.^{4,33} However, knowledge concerning the cooperation of surface metal sites and acid–base sites as well as their respective contributions to the catalytic activity remains ambiguous. In this work, the catalytic activity from Ni/NiAl-MMO(550) to Ni/NiAl-MMO(400) with an enhancement of Ni^0 surface concentration displays a monotonic increase rather than a linear relationship (Figure 7A), suggesting that the metallic Ni as active site is not a single key factor governing the efficiency of catalysts. Moreover, it should be noted that the TOF value (84.4 h^{-1}) for Ni/NiAl-MMO(550) is 1.5 times larger than that for Ni/ Al_2O_3 (55.2 h^{-1}), although their Ni^0 surface concentration ($0.360 \text{ mmol g}^{-1}$ vs $0.364 \text{ mmol g}^{-1}$) and their average size of Ni nanoparticles (8.9 nm vs 9.3 nm) are very close. This further indicates that the dehydrogenation activity of 2-octanol is not just related to the Ni^0 surface concentration; acid–base sites of the supports also play a key role. Notably, the concentration of medium-strong acid–base sites of Ni/NiAl-MMO(550) is significantly larger than that of Ni/ Al_2O_3 , although their total concentration of acid–base sites are almost equal (Table 3). The enhanced performance of Ni/NiAl-MMO can be attributed to medium-strong acid–base sites, which is further demonstrated by the monotonic increase of product formation rate as a function of B_M or A_M from Ni/NiAl-MMO(550) to Ni/NiAl-MMO(400) (Figure 7B,C). The results show that the cooperative catalysis between Ni^0 and medium-strong acid–base sites displays a key role in the dehydrogenation activity of 2-octanol.

Two reaction mechanisms have been proposed for dehydrogenation alcohols: namely, metal alkoxide^{34,35} and alkoxide intermediate,^{4,7,33} respectively. The former normally generates both main product (e.g., secondary, aromatic, or cycloaliphatic ketone) and other byproducts such as alkane, arenes, and cycloparaffins. However, the byproduct formation is negligible in this study; therefore, oxidant-free dehydrogenation of 2-octanol via an alkoxide intermediate over the Ni/NiAl-MMO catalysts is proposed (as shown in Figure 8). The $\text{O}^{\delta-}-\text{H}^{\delta+}$ group in 2-octanol is prone to adsorb on $\text{Ni}^{\delta+}-\text{O}^{\delta-}$ structure (NiO-like phase) with medium-strong acid–base sites as confirmed by CO_2 -TPD and NH_3 -TPD, and the

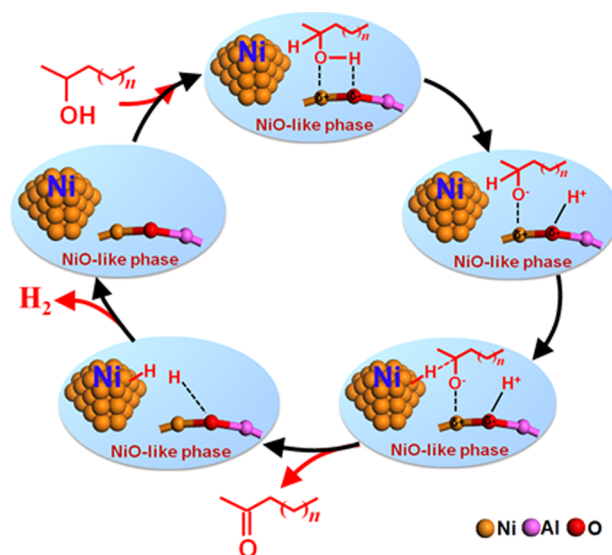


Figure 8. Schematic reaction mechanism for the oxidant-free dehydrogenation of 2-octanol over Ni/NiAl-MMO catalyst.

adsorbed 2-octanol exists in the form of alcoholate intermediate. The cleavage of adsorbed O–H bond produces a surface alkoxy group on the $\text{Ni}^{\delta+}$ site (medium-strong acid site) and a proton on the medium-strong basic $\text{O}^{\delta-}$ site ($\text{Ni}-\text{OH}^{\delta+}$). This step is followed by the cleavage of α -C–H bond in alkoxy group occurring on surface Ni^0 site, which results in $\text{Ni}-\text{H}^{\delta-}$ hydride and 2-octanone. Subsequently, the $\text{Ni}-\text{H}^{\delta-}$ species accepts protolysis from a neighboring $\text{Ni}-\text{OH}^{\delta+}$ to release hydrogen molecule, accompanied by the regeneration of surface Ni^0 site and $\text{Ni}^{\delta+}-\text{O}^{\delta-}$ acid–base sites in NiO-like phase.

Furthermore, operando time-resolved EXAFS spectra at the Ni K-edge were applied to identify the synergic catalysis mechanism between Ni^0 sites and $\text{Ni}^{\delta+}-\text{O}^{\delta-}$ acid–base sites. During the dehydrogenation of 2-octanol reaction at $170 \text{ }^\circ\text{C}$ (Figure 9A), the peak of second Ni–O shell shows a significant increase, which is attributed to the adsorption of $\text{O}^{\delta-}-\text{H}^{\delta+}$ group onto the $\text{Ni}^{\delta+}-\text{O}^{\delta-}$ acid–base sites in NiO-like phase and the formation of $\text{Ni}^{\delta+}$ –alcoholate intermediate. A surface reconstruction of NiO-like phase occurs, resulting in the increased coordination number of second Ni–O shell. In contrast, the peaks of first Ni–Ni shell in Ni^0 decrease markedly in the reaction, which is due to the cleavage of α -C–H bond on its surface and the resulting $\text{Ni}-\text{H}^{\delta-}$ hydride-induced reconstruction of Ni nanoparticles.^{36–38} Therefore, metallic Ni and $\text{Ni}^{\delta+}-\text{O}^{\delta-}$ medium-strong acid–base sites in

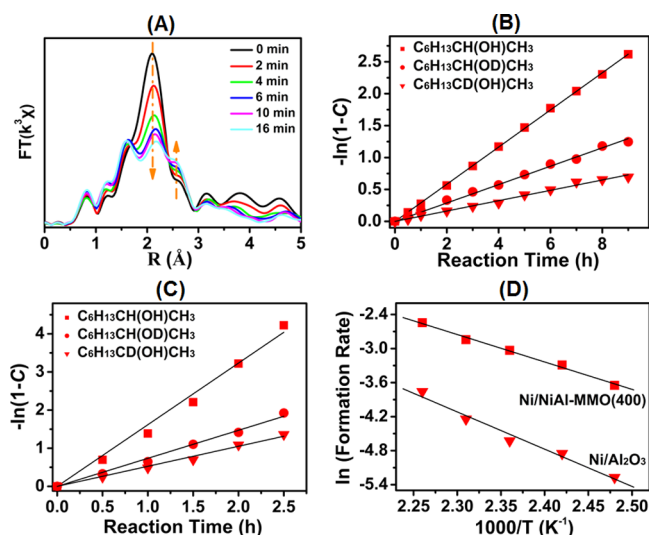


Figure 9. (A) Operando time-resolved EXAFS spectra at the Ni K-edge of Ni/NiAl-MMO(400) in the oxidant-free dehydrogenation of 2-octanol reaction at 170 °C. Kinetic isotope effects in the oxidant-free dehydrogenation of 2-octanol and deuterated 2-octanol using Ni/Al₂O₃ (B) and Ni/NiAl-MMO(400) (C) as catalyst; C represents the conversion of 2-octanol. Reaction conditions: *o*-xylene (6.3 g), 2-octanol or deuterated 2-octanol (6.3 mmol), *n*-dodecane (3.15 mmol), catalyst (0.05 g), 170 °C, 2.5 h, Ar atmosphere. (D) Arrhenius plots for the oxidant-free dehydrogenation of 2-octanol over Ni/Al₂O₃ and Ni/NiAl-MMO(400), respectively. Reaction conditions: *o*-xylene (6.3 g), 2-octanol (6.3 mmol), *n*-dodecane (3.15 mmol), catalyst (0.05 g), 130–170 °C, 2.5 h, Ar atmosphere.

NiO-like phase afford a synergistic catalysis for the dehydrogenation of 2-octanol: α -C–H bond cleavage occurs on surface Ni⁰ site; however, Ni ^{$\delta+$} –O ^{$\delta-$} acid–base sites stabilize the alkoxide intermediate and promote the cleavage of O–H bond.

Kinetic isotope effects (KIE) determination is a very useful method to study the influence of synergistic catalysis on the cleavage of O–H and α -C–H bond in alcohol dehydrogenation. The α -C–H deuterated and O–H deuterated 2-octanol (i.e., C₆H₁₃CD(OH)CH₃ and C₆H₁₃CH(OD)CH₃), respectively, were used in kinetic isotope effects experiments in this work. Figure 9B,C show that the dehydrogenation reactions of C₆H₁₃CH(OH)CH₃, C₆H₁₃CD(OH)CH₃ and C₆H₁₃CH(OD)CH₃ over Ni/NiAl-MMO(400) and Ni/Al₂O₃ give first-order kinetic curves, and the rate constants for the three reactants (k_H , k_{OD} and k_{CD}) are listed in Table S6. Kinetic isotope effects (KIE) values of k_H/k_{OD} and k_H/k_{CD} over Ni/Al₂O₃ are 2.5 and 3.8, respectively, indicating that both O–H and α -C–H bond cleavage are kinetically relevant steps in 2-octanol dehydrogenation (Figure 9B). The latter step tends to control the reaction rate more than the former step. However, the Ni/NiAl-MMO(400) catalyst gives lower k_H/k_{OD} and k_H/k_{CD} values (2.2 and 3.0) than Ni/Al₂O₃ (Figure 9C). This demonstrates that Ni/NiAl-MMO(400) serves as a more efficient catalyst to accelerate the bond cleavage of α -C–H and O–H, resulting in the reduced rate control for these two kinetic steps. Moreover, the apparent activation energy (E_a), associated with the O–H and α -C–H bond cleavage, is estimated from the Arrhenius plots (Figure 9D). The Ni/NiAl-MMO(400) catalyst shows a lower E_a value than Ni/Al₂O₃ (39.2 vs 48.5 kJ mol⁻¹), accounting for its enhanced synergistic catalysis, in agreement with the results of kinetic isotope effects.

3. CONCLUSIONS

In summary, acid–base-promoted Ni nanocatalyst supported on NiAl-MMO was prepared by a precise control over in situ reduction treatment upon the NiAl-LDH precursor. The resulting Ni/NiAl-MMO(400) shows largely enhanced catalytic performance (2-octanone yield of nearly 100% and product formation rate of 78.5 mmol g⁻¹ h⁻¹) for oxidant-free dehydrogenation of 2-octanol. In situ study including XRD, Raman and EXAFS verify that Ni/NiAl-MMO possesses highly dispersed Ni nanoparticles and medium-strong acid–base sites (Ni ^{$\delta+$} –O ^{$\delta-$} pair) located at the NiO-like phase in MMO support. Studies on structure–activity correlation and kinetic isotope effects reveal an enhanced cooperative catalysis between Ni⁰ and medium-strong acid–base sites, in which the former accelerates the α -C–H bond cleavage while the latter facilitates the O–H bond cleavage. Therefore, this work demonstrates an effective strategy to largely improve catalytic performance via enhancing the metal–support synergistic catalysis.

4. EXPERIMENTAL SECTION

4.1. Materials. Analytical grade chemicals including Ni(NO₃)₂·6H₂O, Al(NO₃)₃·9H₂O, NH₄NO₃, sodium tartrate, urea (CO(NH₂)₂), *o*-xylene, 2-octanol, deuterated 2-octanol, *n*-dodecane were supplied by Sigma-Aldrich and used without further purification.

4.2. Synthesis of Ni/NiAl-MMO, NiO/Al₂O₃, and Ni/Al₂O₃ Catalyst. *Synthesis of Ni/NiAl-MMO.* The hierarchical NiAl-LDH precursor was prepared by an in situ growth technique reported by our group.¹⁷ Series Ni/NiAl-MMO catalysts were obtained via the in situ structural topotactic transformation of NiAl-LDH precursor (Ni species content: ~22 wt %) at different temperatures ranging from 400 to 550 °C, using an automatic microreactor with a precise temperature controller. In a typical procedure, 0.1 g of NiAl-LDH precursor was reduced in a flow of 30 vol % H₂/He (30 mL min⁻¹) with a system pressure of 0.05 MPa for 4 h at 400, 450, 500, and 550 °C, respectively. The heating rate was 4 °C min⁻¹. The resulting product was cooled quickly to the room temperature in a He stream (50 mL min⁻¹) for subsequent catalytic evaluation.

Synthesis of NiO/Al₂O₃ and Ni/Al₂O₃. *Synthesis of NiO/Al₂O₃:* NiO/Al₂O₃ as a control sample was prepared by a conventional impregnation method. The amorphous Al₂O₃ support (0.1 g) was dispersed into an aqueous solution of Ni(NO₃)₂·6H₂O (4.8 mol L⁻¹, 0.1 mL). The slurry was stirred at room temperature for 10 h, aged for 24 h, and then dried at 100 °C for 12 h. The obtained solid sample was calcined in air at 450 °C for 4 h, with a heating rate of 4 °C min⁻¹. *Synthesis of Ni/Al₂O₃:* the obtained NiO/Al₂O₃ sample was reduced in a H₂/He (50/50, v/v) stream at 450 °C for 4 h, with a heating rate of 4 °C min⁻¹. The resulting products were fast cooled to the room temperature in a He stream (50 mL min⁻¹) for subsequent catalytic evaluation.

4.3. Characterizations. In situ XRD patterns were measured using a Bruker DAVINCI D8 ADVANCE diffractometer with a MACOR sample cell connected to a gas flow and temperature programming system, with Cu K α source at 40 kV and 250 mA. NiAl-LDH precursor was first reduced in a H₂/He stream at different temperatures ranging from 400 to 550 °C in the MACOR sample cell, followed by flushing (50 mL min⁻¹) with high purity He for 1.0 h. The reduced sample

was slowly cooled to 170 °C (in accordance with reaction temperature) in a He stream, and then the XRD patterns were collected, with a scan step of 0.02° and a 2θ scan range between 5° and 90°. The chemical compositions of prepared samples were determined using a Shimadzu ICPS-7500 inductively coupled plasma–atomic emission spectrometer (ICP–AES). The specific surface area was determined by Brunauer–Emmett–Teller (BET) methods using a Micromeritics ASAP 2020 sorptometer apparatus. In situ Raman spectroscopy was recorded in a Jobin-Yvon LabRam HR800 microscope, excited by a He–Ne green laser (532.14 nm). Hydrogen temperature-programmed reduction (H₂-TPR) was performed on a Micromeritics Auto Chem II 2920 instrument with a thermal conductivity detector (TCD). About 100 mg of sample was loaded in a quartz reactor, and then TPR was carried out with a heating ramp rate of 10 °C min⁻¹ in a gaseous mixture of H₂ and He (1/9, v/v) to a sample temperature of 900 °C, with a total flow rate of 50 mL min⁻¹. CO pulse chemisorption was conducted in a quartz tube reactor on a Micromeritics Auto Chem II 2920 instrument with an online mass spectrometry (MS). In a typical process, 100 mg of sample was first reduced at 400 °C for 1 h in 10 vol % H₂/He, followed by flushing (50 mL min⁻¹) with high purity He for 1.0 h at 410 °C. Afterward, as the temperature declined to 200 K, successive pulses of CO were injected, using He as the carrier gas (50 mL min⁻¹), until a stable mass signal of CO was obtained. Metal dispersion (D%, eq 1) was calculated on the basis of the results of CO pulse chemisorption at 200 K:

$$D\% = \frac{V_{\text{ad}} \times M_{\text{metal}} \times \text{SF}}{m_{\text{cat}} \times \text{wt}\% \times V_{\text{m}}} \times 100 \quad (1)$$

where M_{metal} , m_{cat} , V_{m} , and wt % are the molecular weight of Ni, the weight of sample (g), the molar volume of CO and the weight fraction of Ni, respectively. V_{ad} (mL) is the volume of chemisorbed CO measured in CO pulse chemisorption procedure (Table 1). SF is the stoichiometric factor, which is assumed as 1:1 for CO:Ni. Temperature-programmed desorption (TPD) was carried out using a Micromeritics AutoChem II 2920 apparatus. About 100 mg of sample for either CO₂-TPD or NH₃-TPD test was first reduced at 400 °C for 1 h in 10 vol % H₂/He, followed by flushing (50 mL min⁻¹) with high purity He for 1.0 h at 410 °C. Afterward, as the temperature decreased to 100 °C, either CO₂ or NH₃ was injected until saturation. CO₂-TPD or NH₃-TPD was carried out with a heating ramp rate of 10 °C min⁻¹ to a sample temperature of 500 °C. In situ extend X-ray absorption fine structure spectroscopy (EXAFS) at the Ni K-edge was performed at the beamline 1W1B of the Beijing Synchrotron Radiation Facility (BSRF), Institute of High Energy Physics (IHEP), Chinese Academy of Sciences (CAS). The typical energy of the storage ring was 2.5 GeV with a maximum current of 250 mA. The Si (111) double crystal monochromator was used. The IFFEFIT 1.2.11 data analysis package (Athena, Artemis, Atoms, and FEFF6) was used for the data analysis and fitting. The fitting was performed in r -space after Fourier transformation of the k^3 -weighted data. The k -range was from 2.8 to 13 Å⁻¹. The amplitude reduction factor (S_0^2) was obtained from the experimental EXAFS fitting over NiO reference (25 °C) with known crystallographic value and was fixed to all the samples. Operando time-resolved XAFS measurements were carried out in transmission mode with a time resolution of 2 min. The “steady-state” data were

accumulated by multiple scans (>7) (ca. 15 min each) and merged to improve the signal-to-noise ratio. In a typical process, the powdered sample was first pressed into a sheet and loaded into a reactor cell equipped with polyimide windows. The temperature of the reactor cell was controlled via a precise temperature controller. The sample was reduced at different temperatures ranging from 400 to 550 °C for 1 h in the reactor cell, followed by flushing (50 mL min⁻¹) with high purity He for 0.5 h. The resulting sample was slowly cooled to the reaction temperature (170 °C) in a He stream for 3 h to ensure a stable XAFS signal. Subsequently, the reactant (1% of 2-octanol) was fed into the reactor cell at 170 °C, and operando time-resolved EXAFS spectra at the Ni K-edge were collected at 2, 4, 6, 10, and 16 min, respectively.

4.4. Catalytic Evaluations. The oxidant-free dehydrogenation reaction of alcohols was carried out using a batch-type reactor (cylindrical glass tube), avoiding exposing the catalyst to air. In a typical procedure, 0.05 g of catalyst was dispersed into a mixture of 2-octanol (6.3 mmol), *o*-xylene (6.3 g), and *n*-dodecane (3.15 mmol) in Ar atmosphere. Then, the mixture was stirred under reflux condition at 170 °C. The reactant conversion and product yield were monitored by GC-2014C Shimadzu gas chromatograph (GC) equipped with a flame ionization detector (FID). The products were identified by gas chromatography–mass spectrometry (GC–MS) equipped with the same column as GC. The product formation rate was calculated on the basis of tangent slope of the yield–reaction time plot at the 35% yield of 2-octanone. Turnover frequency (TOF, h⁻¹) was calculated as product formation rate per metallic Ni surface atom.

■ ASSOCIATED CONTENT

📄 Supporting Information

The Supporting Information is available free of charge on the ACS Publications website at DOI: 10.1021/acscatal.6b03494.

TEM images; lattice parameters; in situ XRD patterns; in situ Raman spectra; CO uptake, H₂ consumption, and reduction degree of various catalysts; and other data as mentioned in the text (PDF)

■ AUTHOR INFORMATION

Corresponding Authors

*E-mail for M.W.: weimin@mail.buct.edu.cn. Tel: +86-10-64412131. Fax: +86-10-64425385.

*E-mail for S.H.: vh30@163.com.

ORCID

Min Wei: 0000-0001-7540-0824

Notes

The authors declare no competing financial interest.

■ ACKNOWLEDGMENTS

This work was supported by the 973 Program (Grant No. 2014CB932104), the National Natural Science Foundation of China (NSFC) and the Fundamental Research Funds for the Central Universities (YS 1406). M.W. particularly appreciates the financial aid from the China National Funds for Distinguished Young Scientists of the NSFC. The authors are thankful for the support of the BSRF (Beijing Synchrotron Radiation Facility) during the XAFS measurements.

REFERENCES

- (1) Gunanathan, C.; Milstein, D. *Science* **2013**, *341*, 1229712.
- (2) Mitsudome, T.; Mikami, Y.; Funai, H.; Mizugaki, T.; Jitsukawa, K.; Kaneda, K. *Angew. Chem., Int. Ed.* **2008**, *47*, 138–141.
- (3) Corma, A.; Iborra, S.; Velty, A. *Chem. Rev.* **2007**, *107*, 2411–2502.
- (4) Wang, F.; Shi, R.; Liu, Z. Q.; Shang, P. J.; Pang, X.; Shen, S.; Feng, Z.; Li, C.; Shen, W. *ACS Catal.* **2013**, *3*, 890–894.
- (5) Shimizu, K.; Kon, K.; Seto, M.; Shimura, K.; Yamazaki, H.; Kondo, J. N. *Green Chem.* **2013**, *15*, 418–424.
- (6) Jiang, F.; Zeng, L.; Li, S.; Liu, G.; Wang, S.; Gong, J. *ACS Catal.* **2015**, *5*, 438–447.
- (7) Zhang, M.; Zhao, Y. J.; Liu, Q.; Yang, L.; Fan, G. L.; Li, F. *Dalton Trans.* **2016**, *45*, 1093–1102.
- (8) Enache, D. I.; Edwards, J. K.; Landon, P.; Solsona-Espriu, B.; Carley, A. F.; Herzing, A. A.; Watanabe, M.; Kiely, C. J.; Knight, D. W.; Hutchings, G. J. *Science* **2006**, *311*, 362–365.
- (9) Haider, P.; Baiker, A. *J. Catal.* **2007**, *248*, 175–187.
- (10) Hong, Y. J.; Yan, X. Q.; Liao, X. F.; Li, R. H.; Xu, S. D.; Xiao, L. P.; Fan, J. *Chem. Commun.* **2014**, *50*, 9679–9682.
- (11) Shimizu, K. I.; Kon, K.; Shimura, K.; Hakim, S. S. M. A. *J. Catal.* **2013**, *300*, 242–250.
- (12) Sideris, P.; Nielsen, U.; Gan, Z.; Grey, C. *Science* **2008**, *321*, 113–117.
- (13) Fan, G.; Li, F.; Evans, D. G.; Duan, X. *Chem. Soc. Rev.* **2014**, *43*, 7040–7066.
- (14) He, S.; An, Z.; Wei, M.; Evans, D. G.; Duan, X. *Chem. Commun.* **2013**, *49*, 5912–5920.
- (15) Gao, W.; Li, C.; Chen, H.; Wu, M.; He, S.; Wei, M.; Evans, D. G.; Duan, X. *Green Chem.* **2014**, *16*, 1560–1568.
- (16) He, L.; Huang, Y.; Wang, A.; Wang, X.; Chen, X.; Delgado, J. J.; Zhang, T. *Angew. Chem., Int. Ed.* **2012**, *51*, 6191–6194.
- (17) He, S.; Li, C.; Chen, H.; Su, D.; Zhang, B.; Cao, X.; Wang, B.; Wei, M.; Evans, D. G.; Duan, X. *Chem. Mater.* **2013**, *25*, 1040–1046.
- (18) Kong, X.; Zheng, R.; Zhu, Y.; Ding, G.; Zhu, Y.; Li, Y. W. *Green Chem.* **2015**, *17*, 2504–2514.
- (19) Abelló, S.; Verboekend, D.; Bridier, B.; Pérez-Ramírez, J. *J. Catal.* **2008**, *259*, 85–95.
- (20) Rudolf, C.; Dragoi, B.; Ungureanu, A.; Chirieac, A.; Royer, S.; Nastro, A.; Dumitriu, E. *Catal. Sci. Technol.* **2014**, *4*, 179–189.
- (21) He, L.; Huang, Y.; Wang, A.; Liu, Y.; Liu, X.; Chen, X.; Delgado, J. J.; Wang, X.; Zhang, T. *J. Catal.* **2013**, *298*, 1–9.
- (22) Pérez-Ramírez, J.; Mul, G.; Moulijn, J. A. *Vib. Spectrosc.* **2001**, *27*, 75–88.
- (23) Wang, W. Z.; Liu, Y. K.; Xu, C. K.; Zheng, C. L.; Wang, G. H. *Chem. Phys. Lett.* **2002**, *362*, 119–122.
- (24) Ghule, A. V.; Ghule, K.; Punde, T.; Liu, J. Y.; Tzing, S. H.; Chang, J. Y.; Chang, H.; Ling, Y. C. *Mater. Chem. Phys.* **2010**, *119*, 86–92.
- (25) Chan, S. S.; Wachs, I. E. *J. Catal.* **1987**, *103*, 224–227.
- (26) Peck, M. A.; Langell, M. A. *Chem. Mater.* **2012**, *24*, 4483–4490.
- (27) Liu, P.; Derchi, M.; Hensen, E. J. M. *Appl. Catal., A* **2013**, *467*, 124–131.
- (28) Dębek, R.; Radlik, M.; Motak, M.; Galvez, M. E.; Turek, W.; Da Costa, P.; Grzybek, T. *Catal. Today* **2015**, *257*, 59–65.
- (29) Díez, V. K.; Apesteguía, C. R.; Di Cosimo, J. I. *J. Catal.* **2006**, *240*, 235–244.
- (30) Na, K.; Alayoglu, S.; Ye, R.; Somorjai, G. A. *J. Am. Chem. Soc.* **2014**, *136*, 17207–17212.
- (31) McFarland, E. W.; Metiu, H. *Chem. Rev.* **2013**, *113*, 4391–4427.
- (32) Heracleous, E.; Lemonidou, A. A. *J. Catal.* **2010**, *270*, 67–75.
- (33) Zaccheria, F.; Ravasio, N.; Psaro, R.; Fusi, A. *Chem. - Eur. J.* **2006**, *12*, 6426–6431.
- (34) Davis, S. E.; Ide, M. S.; Davis, R. J. *Green Chem.* **2013**, *15*, 17–45.
- (35) Ning, X.; Li, Y.; Yu, H.; Peng, F.; Wang, H.; Yang, H. *J. Catal.* **2016**, *335*, 95–104.
- (36) Wang, J. Q.; Wang, Q.; Jiang, X. H.; Liu, Z. N.; Yang, W. M.; Frenkel, A. I. *J. Phys. Chem. C* **2015**, *119*, 854–861.
- (37) Mager-Maury, C.; Bonnard, G.; Chizallet, C.; Sautet, P.; Raybaud, P. *ChemCatChem* **2011**, *3*, 200–207.
- (38) Paredis, K.; Ono, L. K.; Mostafa, S.; Li, L.; Zhang, Z. F.; Yang, J. C.; Barrio, L.; Frenkel, A. I.; Cuenya, B. R. *J. Am. Chem. Soc.* **2011**, *133*, 6728–6735.